Received: 5 March 2019 | Revised: 25 July 2019 | Accepted: 29 July 2019

DOI: 10.1002/mrm.27955

FULL PAPER

Magnetic Resonance in Medicine

Time optimal control-based RF pulse design under gradient imperfections

Christoph S. Aigner[1] | **Armin Rund**[2] | **Samy Abo Seada**[3] | **Anthony N. Price**[3] | **Joseph V. Hajnal**[3] | **Shaihan J. Malik**[3] | **Karl Kunisch**[2,4,5] | **Rudolf Stollberger**[1,5]

[1]Institute of Medical Engineering, Graz University of Technology, Graz, Austria

[2]Institute for Mathematics and Scientific Computing, University of Graz, Graz, Austria

[3]School of Biomedical Engineering and Imaging Sciences, King's College London, London, United Kingdom

[4]Johann Radon Institute for Computational and Applied Mathematics (RICAM), Austrian Academy of Sciences, Linz, Austria

[5]BioTechMed-Graz, Graz, Austria

Correspondence
Christoph S. Aigner, Graz University of Technology, Institute of Medical Engineering, Stremayrgasse 16/III, A-8010 Graz, Austria.
Email: christoph.aigner@gmail.com

Funding information
Austrian Science Fund, Grant/Award Number: SFB F32-N18; Centre for Medical Engineering at King's College London, Grant/Award Number: WT 203148/Z/16/Z; King's College London & Imperial College London EPSRC Centre for Doctoral Training in Medical Imaging, Grant/Award Number: EP/L015226/1 and EP/L00531X/1; ERC, Grant/Award Number: 668998

Purpose: This study incorporates a gradient system imperfection model into an optimal control framework for radio frequency (RF) pulse design.

Theory and Methods: The joint design of minimum-time RF and slice selective gradient shapes is posed as an optimal control problem. Hardware limitations such as maximal amplitudes for RF and slice selective gradient or its slew rate are included as hard constraints to assure practical applicability of the optimized waveforms. In order to guarantee the performance of the optimized waveform with possible gradient system disturbances such as limited system bandwidth and eddy currents, a measured gradient impulse response function (GIRF) for a specific system is integrated into the optimization.

Results: The method generates optimized RF and pre-distorted slice selective gradient shapes for refocusing that are able to fully compensate the modeled imperfections of the gradient system under investigation. The results nearly regenerate the optimal results of an idealized gradient system. The numerical Bloch simulations are validated by phantom and in-vivo experiments on 2 3T scanners.

Conclusions: The presented design approach demonstrates the successful correction of gradient system imperfections within an optimal control framework for RF pulse design.

KEYWORDS
gradient imperfections, gradient impulse response function, pulse design, simultaneous multi-slice excitation, time optimal control

1 | INTRODUCTION

MRI can be effectively accelerated by fast sequences[1] or parallel imaging strategies in combination with advanced reconstruction techniques.[2,3] In addition to in-plane parallel imaging, simultaneous encoding and acquisition of multiple slices (SMS) were shown to further increase the temporal efficiency of various clinically relevant MR sequences.[4,5]

Basic SMS radio frequency (RF) pulses can be computed by a simple superposition of conventional single slice RF pulses with different carrier frequencies.[6] This superposition, however, comes with the burden of a linear scaling of the maximal peak RF amplitude. To fulfill RF peak constraints, such SMS pulses are therefore typically stretched over long pulse durations. This can lead to conflicts with the achievable multiband (MB) factor, minimal echo time T_E, and echo spacing.[5] The increased T_E easily becomes a limiting issue for spin echo (SE) based applications such as turbo spin echo[7] or high resolution diffusion imaging.[8] Therefore, different RF pulse design methods have been introduced to reduce peak RF amplitudes[9-11] or RF power by applying variable-rate slice selective excitation (VERSE)[12-17] or power independent number of slices (PINS).[18,19]

Alternatively, SMS RF pulses can be computed via optimal control.[20-22] A refined optimal control model and method for the joint design of RF and slice selective gradient (G_s) shapes with the inclusion of all relevant hardware constraints as hard constraints was recently introduced.[21] An extension of this optimal control method for the design of minimum duration pulses was presented in.[22] These time optimal solutions not only fully exploit prescribed constraints on the designed waveforms such as RF and slice selective gradient peak amplitudes or slew rate limitations as well as slice profile and phase accuracy but also result in strongly time-varying G_s shapes.

Time-variable gradients are known to be prone to gradient imperfections, including eddy currents with very long or short time constants, time delays, or bandwidth limited gradient amplifier that potentially limit their application. The linear time-invariant gradient impulse response function (GIRF) has been shown to sufficiently assess the gradient performance[23] for the correction of k-space trajectory alterations in image reconstruction[24] and pTx pulse design.[25]

In this work, we show that a direct inclusion of the GIRF in a time optimal control framework[22] enables the design of short RF and G_s shapes for SMS refocusing that inherently correct for measured gradient system imperfection. The proposed design method was tested via various SMS refocusing examples for a wide range of parameters. Additionally, phantom and in-vivo data was acquired on 2 3T systems.

2 | THEORY

This section contains the description of the GIRF, its impact on the numerical Bloch simulations as well as its inclusion in the time optimal control framework.[22]

2.1 | Gradient impulse response function

Linear and time-invariant (LTI) effects of the gradient system, including influences arising from the gradient amplifier, gradient coil as well as eddy currents and mechanical vibrations, can be characterized by the gradient impulse response function (GIRF).[23]

At this point, it is important to distinguish between the gradient amplitude G_s that is included in the MR sequence, and its GIRF filtered version $\tilde{G}_s$ that is realized by the gradient system. Let $h(t)$ be the GIRF that relates these 2 functions via a convolution in the time domain

$$\tilde{G}_s(t) = G_s(t) * h(t). \tag{1}$$

With known GIRF this equation allows an accurate prediction of the gradient field amplitude $\tilde{G}_s$ that is produced inside of the MR bore. Alternatively, the convolution operation can be applied in the frequency domain by multiplying the Fourier transform of the GIRF H with the Fourier transform of G_s

$$\tilde{G}_s = \Re(\mathcal{F}^{-1} H \mathcal{F} G_s), \tag{2}$$

with $H = \mathcal{F}[h]$, the Fourier transform $\mathcal{F}$ and its inverse $\mathcal{F}^{-1}$. In the discrete setting, $\mathcal{F}^{-1}, H, \mathcal{F}$ are matrices whose dimensions and entries depend on the frequency resolution δ_f and bandwidth of H as well as the time resolution τ and pulse duration T of G_s. It should be noted that given by definition the LTI assumption does not account for non-linear[26] or time-variable temperature dependences.[27] We also restrict ourselves to the distortion on each gradient axis due to its own application, excluding cross terms, higher order spatial terms or B_0 variations.

2.2 | Optimal control framework

The following optimal control framework is based on our preceding work,[21,22] which assumed an idealized gradient system model. We demonstrate how the inclusion of a refined GIRF-based model can compensate for gradient imperfections and enhance the precision of the optimized pulses in practical applications. The key challenge for this is the inclusion of the GIRF into the optimal control model in order to fully profit from the optimization process. In particular, we pose the hardware constraints to the demand gradient waveform G_s whereas the Bloch equation prediction and evaluation applies to the realized or GIRF filtered gradients $\tilde{G}_s$.

The numerical simulations are based on the spin domain Bloch equations with neglected relaxation terms. An uniform time grid is applied with N_t time points for time $t \in [0, T]$ with a time step size $\tau = T/(N_t - 1)$. A piecewise constant discretization for the complex-valued RF, for the real-valued G_s and real-valued $\tilde{G}_s$ is applied with values $B_{1,m}$, $G_{s,m}$, $\tilde{G}_{s,m}$ for $m = 1, \ldots, N_t - 1$. In particular, Equation 2 is converted into a discretized matrix form $\tilde{G}_{s,m} = \Re(F^{-1}HF)G_{s,m}$ and polar coordinates are used for $B_{1,m} = r_m \exp(i\vartheta_m)$ that allows direct description of the peak RF amplitude constraint with given matrices F, H specified in the experiments below.

The RF pulse design framework is completely general. However, since the focus of this work is to explore methods which include limitations in gradient performance, we limited the experimental design to real valued RF pulses and assumed an ideal RF hardware system.

The temporal evolution of the magnetization vector is solved by a series of complex rotation matrices based on the Cayley-Klein parameters[28,29] a_m and b_m

$$a_m = \alpha_m a_{m-1} - \beta_m^* b_{m-1}, \tag{3}$$

$$b_m = \beta_m a_{m-1} + \alpha_m^* b_{m-1}, \tag{4}$$

running from $m = 1, \ldots, N_t$ with the initialization $a_0 = 1$ and $b_0 = 1$ and coefficients

$$\alpha_m = \cos(\phi_m/2) + i\gamma\tau z\tilde{G}_{s,m}\sin(\phi_m/2)/\phi_m, \tag{5}$$

$$\beta_m = i\gamma\tau B_{1,m}\sin(\phi_m/2)/\phi_m, \tag{6}$$

$$\phi_m = -\gamma\tau\sqrt{r_m^2 + (z\tilde{G}_{s,m})^2}, \tag{7}$$

at spatial location z and the gyromagnetic ratio γ.

The prescribed magnitude and phase constraints are evaluated assuming a perfectly crushed SE refocusing profile $b_{N_t}(z)^2$ [29]in a pointwise manner for a given field of view (FOV) in the slice direction consisting of N_z spatial points $z \in [-FOV/2, FOV/2]$ using an equidistant spatial resolution $\delta = FOV/N_z$. Following[21] the slice profile accuracy is modeled as small deviation from the ideal profile

$$|b_{N_t}|^2 \le e_{\text{out}}(z) \quad \forall z \in \Omega_{\text{out}}, \qquad 1 - |b_{N_t}|^2 \le e_{\text{in}}(z) \quad \forall z \in \Omega_{\text{in}}, \tag{8}$$

where Ω_{out} and Ω_{in} are the domain parts out-of-slice and in-slice, and e_{out}, e_{in} are their respective error bounds. Moreover, the phase spread inside each slice is desired to be nearly constant

$$|\varphi - \bar{\varphi}_l| \le e_{\text{p}}(z), \quad \forall l = 1, \ldots, N_s \tag{9}$$

with mean phase $\bar{\varphi}_l$ of slice l out of the N_s slices.

Besides slice profile constraints, the optimized RF pulses and gradient shapes need to fulfill technical constraints of the MR scanner hardware. Among these are amplitude constraints on the RF pulse, the pre-emphasized G_s shape and its slew rate s_m, which are essential to pass the hardware checks.

$$0 \le r_m \le r_{\max}, \qquad G_{s,m} \le G_{\max}, \qquad |s_m| \le s_{\max}, \qquad -\pi \le \vartheta_m \le \pi. \tag{10}$$

2.3 | Optimal control method

The aim of the optimal control method is to optimize for the control $\mathbf{x} = (r_1, \ldots, r_{N_t-1}, \vartheta_1, \ldots, \vartheta_{N_t-1}, s_1, \ldots, s_{N_t-1})$ and the free terminal time $T > 0$ in order to minimize the cost function

$$\begin{aligned}\min_{T>0,\mathbf{x}} J = T &+ \frac{\tau\mu_{RF}}{2}\sum_{time}|B_{1,m}|_2^2 + \frac{\tau\mu_G}{p}\sum_{time}\left(\frac{G_{s,m}}{G_{\max}}\right)^p \\ &+ \frac{\delta\mu_{\text{out}}}{2p}\sum_{outslice}\left(\frac{|b_{N_t}|^2}{e_{\text{out}}}\right)^p + \frac{\delta\mu_{\text{in}}}{2p}\sum_{inslice}\left(\frac{|b_{N_t}|^2 - 1}{e_{in}}\right)^p \\ &+ \frac{\delta\mu_{\text{p}}}{p}\sum_{slices}\sum_{inslice}\left(\frac{\varphi - \bar{\varphi}_l}{e_p}\right)^p\end{aligned} \tag{11}$$

subject to Equations (3-7) and

$$0 \le r_m \le r_{\max}, \qquad |s_m| \le s_{\max}, \qquad -\pi \le \vartheta_m \le \pi, \tag{12}$$

$$\tilde{G}_{s,m} = \Re(F^{-1}HF)G_{s,m}. \tag{13}$$

Therein, the first 2 terms of Equation 11 constitute the time- and energy-optimal cost function with weight $\mu_{RF} > 0$. The other terms are L^p-penalization terms of the inequality constraints on the state variables where the exponent p is an positive even number ($P > 2$) that is increased throughout the optimization to achieve L^∞ like error behavior. The regularization parameters $\mu_{RF}, \mu_G, \mu_{\text{out}}, \mu_{\text{in}}, \mu_p > 0$ are adapted after every 20th optimization step to ensure balanced penalty terms.[21] This penalization method is needed here for coping with general inequality constraints. In contrast, the hardware limits on the controls Equation 12 can be included efficiently by projection-based semismooth Newton/quasi-Newton methods without increasing the computational effort or introducing additional parameters. For detailed background on the treatment of the inequality constraints in this context we refer to.[21,22]

The maximal slice selective gradient amplitude $G_{\max}$ and, the error bounds on the slice profile accuracy e_{in}, e_{out} and the slice profile phase e_p normalize the deviation to the desired state. For the sake of simplicity $e_s = \max(e_{\text{in}}, e_{\text{out}})$ will be used later on to define the magnitude error of e_{in}, e_{out}. Additionally, we track the SAR estimate (W/kg)

$$SAR_e = \text{SAR}_{\text{coileff}} f_p \tau \sum_{m=1}^{N_t} r_m^2, \tag{14}$$

with a constant pulse rate f_p (1/s) and coil efficiency $\mathrm{SAR}_{\mathrm{coileff}}$ (W/kg/μT^2)[8] that impacts the weighting of μ_{RF}.

The optimization is done with the bilevel method for time optimal control as presented in our previous work.[22] In particular, the lower level problem is solved for a fixed pulse duration employing adjoint-based exact first derivatives and second derivatives supplied by a hybrid semismooth Newton/quasi-Newton method with Broyden-Fletcher-Goldfarb-Shanno (BFGS) update.[21] To extend the bilevel method to the GIRF inclusion, the linear transformation Equation 13 is added prior to the Bloch simulation. According to the chain rule, this change is consistently transferred to the first derivatives.

3 | METHODS

This section describes the implementation and details of the proposed pulse design and the performed experimental validation.

3.1 | Experimental setup

The methods described in this paper have been tested using 2 separate Philips 3T MR systems (both Achieva). Scanner 1 has an experimental 8-channel body coil[30] with scan software capable of GIRF measurement using an image-based procedure similar to.[31] Scanner 2 is a standard clinical system with 2-port birdcage transmitter with software implementation of SMS imaging techniques. Since neither system had both capabilities, SMS imaging was performed by scanner 2 using pulses corrected for the GIRF measured from scanner 1. Though not ideal, prior experience suggests that the gradient performance of both systems is similar[17]; errors that may arise from assuming this equivalence will be discussed later.

Figure 1 depicts the idealized (H_i) and the measured transfer functions along the y (H_y) and z (H_z) direction with frequency resolution $\delta_f = 76.3$ Hz. The 2 measured GIRFs both have low-pass characteristics but differ in cutoff frequency (4200 Hz for H_y and 3750 Hz for H_z) where the magnitude response is reduced by a factor of $1/\sqrt{2}$. Moreover, the phase deviation potentially leads to a varying phase shift of different frequency components. The GIRF data and details about its application are publicly available (https://github.com/mriphysics/reVERSE-GIRF).

3.2 | Pulse design

The presented optimization approach is an extension of our preceding work[22] that can be downloaded from https://github.com/rundar/mr.control. The algorithm was implemented in MATLAB (The MathWorks, Inc., Natick) with pre-compiled C-based MEX files for an accelerated parallel solution (OpenMP) of all Bloch simulations and derivative computations. All calculations were done in parallel on the high-performance computing cluster "RADON 1" (RICAM, Linz, Austria) using 1 node (2x Xeon E5-2630v3 with in total 16 cores and 128 GB of RAM) for each case. All shown examples were designed for SMS refocusing assuming perfect spoiling with varying multiband factor (MB), time-bandwidth-product (TBWP), slice-thickness (THK) and field of view (FOV). The global head SAR estimate SAR_e, see Equation 14, was computed with a fixed pulse frequency $f_p = 16.67$ 1/s and SAR efficiency $\mathrm{SAR}_{\mathrm{coileff}} = 0.25$ W/kg/μT^2 for a representative 3T birdcage coil.[8] As testing was performed on the brain (see below), we adopted the head SAR limit of $\mathrm{SAR}_{\max} = 3.2$ W/kg.

The hardware constraints on the amplitudes of the RF $r_{\max} = 13$ μT, slice selective gradient $G_{\max} = 30$ mT/m and its slew rate $s_{\max} = 180$ T/m/s were chosen to comply with the experiments on Philips Achieva 3T MR systems with maximal hardware limits of 40 mT/m and 200 T/m/s (Philips Healthcare, Best, Netherlands). Additionally, the time discretization of the RF and G_s shapes was set to the minimal gradient raster time $\tau = 6.4$ µs of the previously mentioned MR systems and remains constant throughout the optimization. The iterative bilevel optimization was always initialized according to our preceding work,[22] with PINS[18] RF and G_s shapes based on a SLR[29] sub-pulse assuming a perfectly crushed SE with the parameters $d_1 = 0.01/4$ and $d_2 = 0.01/\sqrt{2}$. The resulting initial pulse durations ranged from $T = 7.48$ ms (MB = 3, TBWP = 2, THK = 2 mm and FOV = 120 mm) to $T = 24.67$ ms (MB = 5, TBWP = 4,

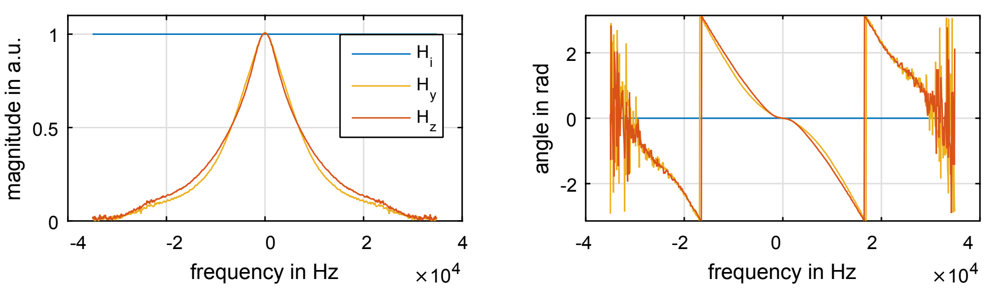

FIGURE 1 Magnitude and phase angle of the idealized (H_i) and measured GIRF in y (H_y) and z-direction (H_z)

THK = 1 mm and FOV = 120 mm). The error bounds of the deviation from the ideal refocusing profile were set to $e_s = 1-3\%$.

One set of parameters (MB = 4, TBWP = 4, THK = 2 mm and FOV = 120 mm) was analyzed and compared in more detail to examine the impact of an idealized and measured GIRF on the proposed pulse design. For this purpose, we optimized 2 scenarios using the ideal unit response (H_i) and the measured GIRF along the z-direction (H_z). Both optimization runs were initialized with the same PINS pulse. The 3 pulse candidates were evaluated and, following GIRF application (H_i and H_z), were additionally compared with Bloch simulations. To examine the effect of time-invariant B_0 and B_1 inhomogeneities on the optimized RF and $\tilde{G}_s$ shapes we computed Bloch simulations with a B_1 scaling of 75-125% B_1 and an off-resonance range of $\Delta B_0 = \pm 200$ Hz. The impact of ΔB_1 and ΔB_0 on the refocusing profile was analyzed for 2 representative slices.

A second set of parameters (MB = 5, TBWP = 4, THK = 2 mm and FOV = 120 mm) was analyzed with different assumptions regarding phase constraints and using different GIRFs in pulse design and evaluation. Firstly, optimization was performed with and without constraints on the phase angle of the refocusing profile. For the former, the maximum allowed deviation of the phase angle from the mean phase was $e_s = 0.25$ rad per slice. In all other optimization scenarios, unless stated otherwise, explicit phase angle constraints were included to reduce the phase spread of the refocusing profiles. Secondly, we tested the effect of assuming an ideal gradient system (H_i). We then evaluated the optimized pulse and G_s shape with measured GIRFs of different gradient directions (H_z, H_y and H_{yz}) with H_{yz} being the arithmetic mean of H_z and H_y. Thirdly, we analyzed the impact of using different gradient axes in optimization and evaluation (H_z, H_y and H_{yz}).

To test the influence of TBWP, MB, THK, and FOV on the proposed optimization method, pulses were computed for different parameter combinations (MB = 3-8, TBWP = 2-4, THK = 1-5 mm and FOV = 90-210 mm). The optimization was done with phase angle constraints for the ideal unit response (H_i) and measured GIRF (H_z).

3.3 | Experimental validation

The numerical simulations were validated by phantom measurements using an 8-channel head coil on scanner 1. Using 3 MB factors (MB = 3, 4 and 5), phantom measurements were performed to measure the slice profile of a crushed SE sequence. All other parameters (TBWP = 4, THK = 2 mm, FOV = 120 mm, $e_s = 1\%$ and $e_p = 0.025$ rad) were identical. For each MB factor 2 sequences were created using H_i and H_z optimized results. For excitation we computed SLR[29] based phase optimized superposition MB pulses with matching slice profiles.[32] The measurements of the slice profile were performed along the z-direction (transversal) for a homogeneous bottle phantom filled with mineral oil. The sequence parameters were set to $T_E/T_R = 16/100$ ms, FOV = 140 × 140 mm, in-plane resolution = 0.5 × 0.5 mm, matrix = 1024 × 1024). The slice profile measurements were corrected by an intensity profile of a sagittal single slice GRE reference measurement (THK = 2 mm) with the same sequence parameters.

In vivo scans of a healthy male volunteer were conducted using the same 8-channel head coil on scanner 2.[17] Two optimized H_i and H_z RF pulses (MB = 4, TBWP = 4, THK = 2 mm, FOV = 120 mm, $e_s = 1\%$, $e_s = 0.025$ rad) were scaled down by a factor of 9 to be used as low tip angle excitation pulses. The scaling was carried out only for the purpose of experimental demonstration. The optimized slice selective gradient shapes were adopted without alterations. Two GRE sequences with blipped-CAIPI shift were created with $T_E/T_R = 11/200$ ms, FOV = 240 × 240 mm, in-plane resolution = 0.75 × 0.75 mm, matrix = 480 × 480, CAIPI shift = 3. The aliased MB data were reconstructed with a SENSE-based algorithm using ReconFrame (GyroTools GmbH, Zürich, Switzerland).

4 | RESULTS

This section demonstrates the compensation of gradient system imperfections for time optimal SMS refocusing with highly varying G_s shapes with numerical simulations and experimental phantom and in vivo measurements on a 3T MR system.

4.1 | Simulations

The 3 columns in Figure 2 correspond to the PINS initial, H_i and H_z optimized results. Descending the RF and slew rate of G_s together with G_s and the filtered $\tilde{G}_s^{H_z}$ shapes and the corresponding simulated refocusing profiles (MB = 4, TBWP = 4, THK = 2 mm and FOV = 120 mm) are displayed. The overall duration of the optimized results reduced from 17.41 ms (PINS initial) to 3.46 ms (optimized assuming an ideal uniform response H_i) and 3.78 ms (optimized with the measured GIRF along the z-direction H_z). The point-wise constraints on the RF and G_s amplitudes as well as on the refocusing profile are depicted by black dotted lines. It can be seen that the optimized RF and G_s waveforms often attain the bound constraints for the control variables (RF amplitude and G_s slew rate). Although not shown, the optimization runs were performed with explicit constraints on the phase spread of the refocusing profiles ($e_p = 0.025$ rad). The simulated refocusing profiles for the G_s and $\tilde{G}_s^{H_z}$ shapes of the PINS initial resulted in a slice shift of 0.2 mm for the outermost slice, see bottom row of Figure 2. In contrast, the impact of H_z on the G_s waveform was

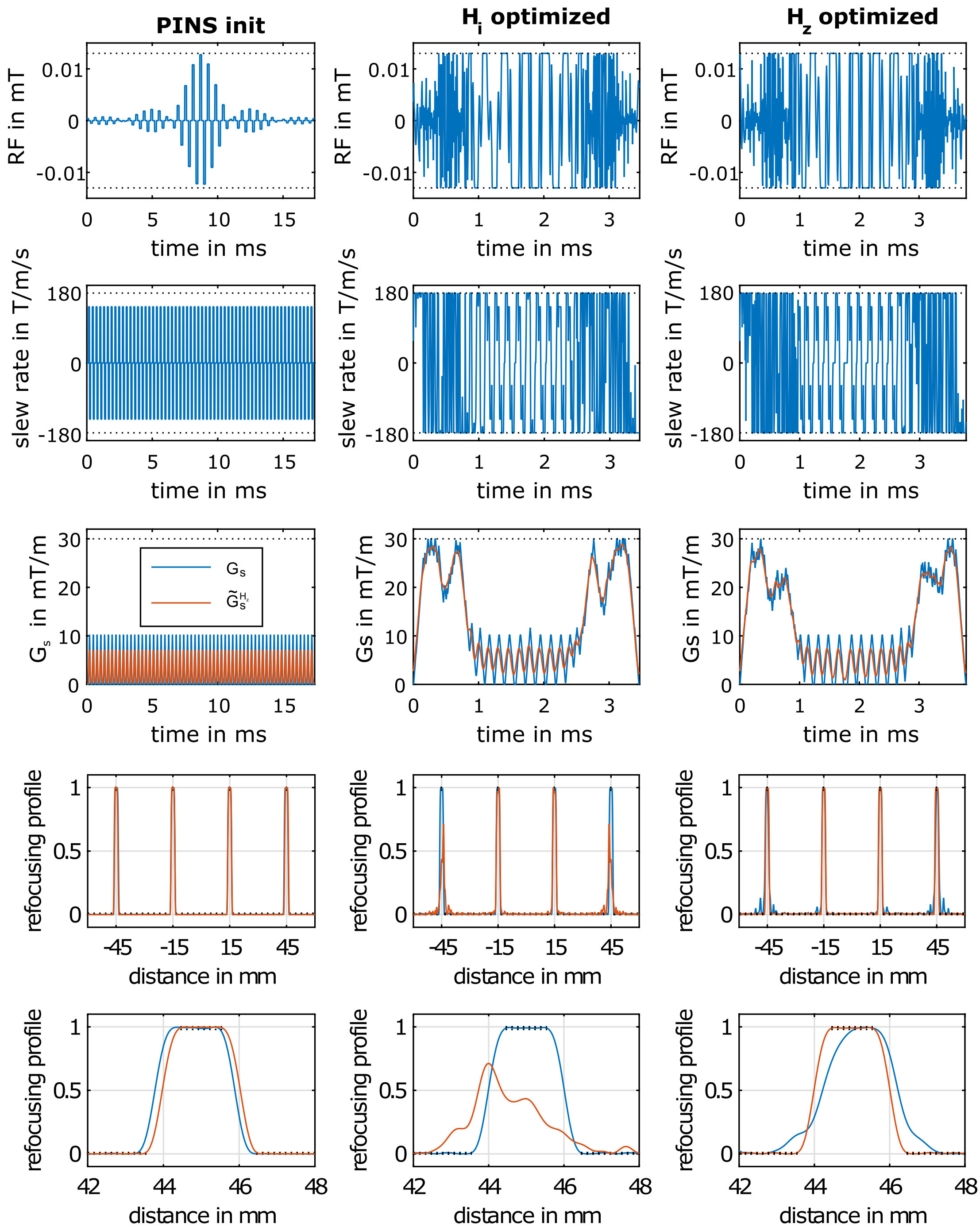

FIGURE 2 Impact of the measured GIRF H_z, see Figure 1, on 3 different slice selective gradient shapes and simulated refocusing profiles. Column 1 depicts the PINS initial used as an educated guess to initialize the H_i (column 2) and H_z (column 3) optimization (with constraints on the phase angle of the refocusing profile). Row 1 depicts the RF pulse and row 2 depicts the slew rate of the slice selective gradient. Row 3 depicts the slice selective gradient shapes before (G_s in blue) and after convolution with the H_z GIRF ($\tilde{G}_s^{H_z}$ in orange) together with the magnitude constraints (dotted black). Rows 4 and 5 show the simulated refocusing profiles $|b_{N_t}(z)|^2$ before (blue) and after convolution with the H_z GIRF (orange) together with the spatial magnitude constraints (dotted black). Note that in the center column the blue curve performs as expected and the orange curve shows substantial damage. In the third column the reverse is the case, with the orange curve following the desired performance

considerably more pronounced for the optimized cases. The fourth row depicts the slice profiles either without filtering (blue curve, using H_i) or with realistic H_z filtering (orange curve). The classical optimized case (column 2) results in distorted refocusing profiles for $\tilde{G}_s^{H_z}$ (orange curve). This is most noticeable in row 5, which displays a magnified view of the outermost slice. Inclusion of H_z in the optimization led to complete compensation of slice profile degeneration,

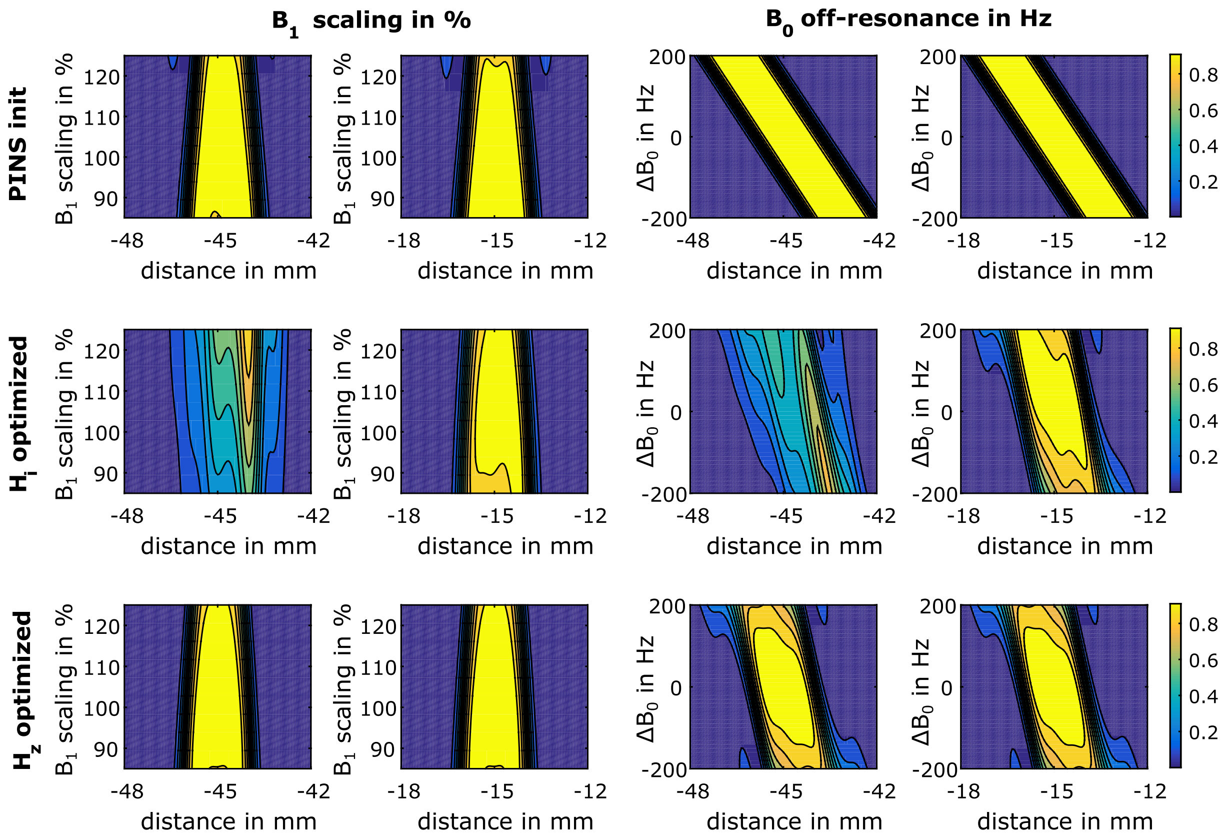

FIGURE 3 Simulated refocusing profiles $|b_{N_t}(z)|^2$ for a variation in the B_0 off-resonance and B_1 inhomogeneity using the H_z filtered slice selective gradient shapes $\tilde{G}_s^{H_z}$ shown in Figure 2. Columns 1 and 3 show a magnified view of to the outermost slice and columns 2 and 4 show a magnified view to a central slice. The other 2 slices result in similar refocusing patterns

as seen in column 3, where the simulated refocusing profile (orange line) precisely fulfills the prescribed constraints on the refocusing profile.

Figure 3 depicts refocusing profiles for a B_1 variation of 85-125% (column 1 and 2) and B_0 offset range of ±200 Hz (column 3 and 4) for 2 representative slices. The other 2 slices showed similar results. The simulations were performed with the $\tilde{G}_s^{H_z}$ shapes shown in Figure 2. The inclusion of the realistic H_z filtering in the last row improves the slice profiles over the entire simulated B_0/B_1 range, especially for the outermost slice.

Figure 4 compares the impact of constrained phase angles of the refocusing profiles for 1 representative example (MB = 5, TBWP = 4, THK = 2 mm, FOV = 120 mm, $e_s = 2\%$). Row 1 shows the H_z optimized result without phase angle constraints and row 2 shows the H_z optimized result with an allowed phase deviation $e_p = 0.025$ rad. There are only minor differences in the magnitude of the refocusing profiles (column 2). The consideration of the phase angle, however, resulted in a much less pronounced phase deviation with slightly longer pulse durations (3.69 ms compared to 3.58 ms without a phase angle constraint).

Next, we investigated the impact of different slice orientations. Figure 5 shows the H_z optimized example of Figure 4 filtered with H_y (column 1) and an optimized example using an averaged transfer function (H_{yz}) filtered with H_y (column 2) and H_z (column 3). The appearance of the different gradient shapes was similar across all optimized results. Regarding the different gradient directions, only small changes were observed for the simulated slice profiles. Again, the differences were less pronounced for the central slices.

Table 1 summarizes the performance of optimized pulse candidates (MB = 5) for different gradient directions with and without explicit phase constraints for different GIRF directions. The table compares maximal slice (e_s) and phase errors (e_p) of the refocusing profile using the H_z filtered slice selective gradient $\tilde{G}_s^{H_z}$, SAR estimates SAR_e and the pulse duration T. The maximal refocusing profile deviation increases, compared to the 2% refocusing error constraint used in the optimization, to roughly 18% for the H_y optimized case evaluated with the H_z GIRF. The use of an averaged GIRF H_{yz} in the optimization results in an intermediate case with a low slice profile error for both gradient directions. The evaluation of the refocusing accuracy with respect to H_y and H_{yz} is summarized in Supporting Information Table S1.

Finally, we investigated the influence of different parameters (TBWP, MB, THK, and FOV) on the proposed

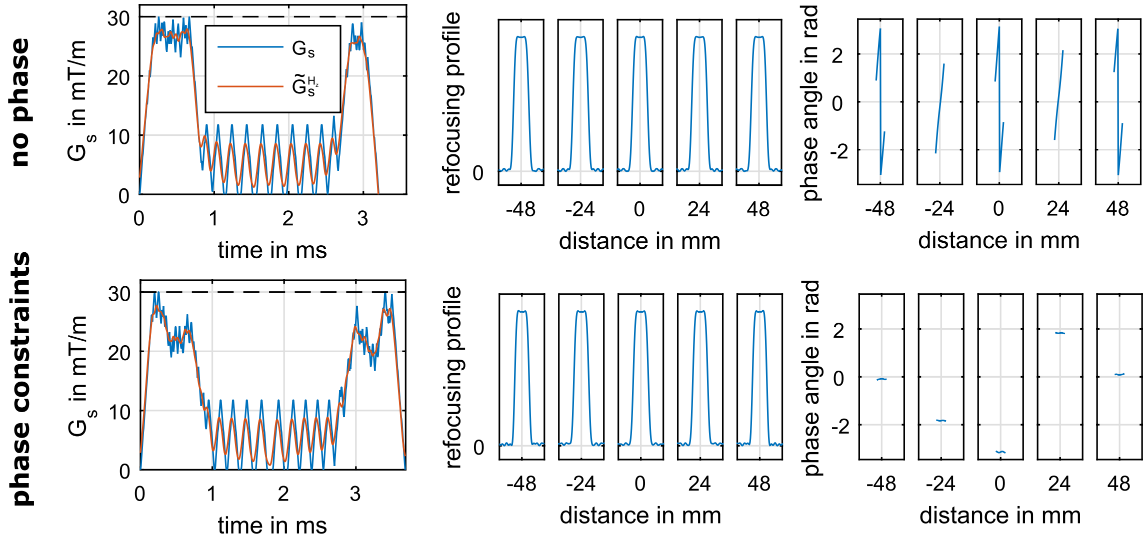

FIGURE 4 Comparison of 2 H_z GIRF optimized MB = 5 examples with and without a distinct constraint on the phase spread of the refocusing profile with otherwise identical parameters. Column 2 shows an enlargement of 6 mm to demonstrate the simulated refocusing profiles $|b_{N_t}(z)|^2$ and Column 3 shows an enlargement of 6 mm to see the phase spread $\arg(b_{N_t}(z)^2)$ of each slice

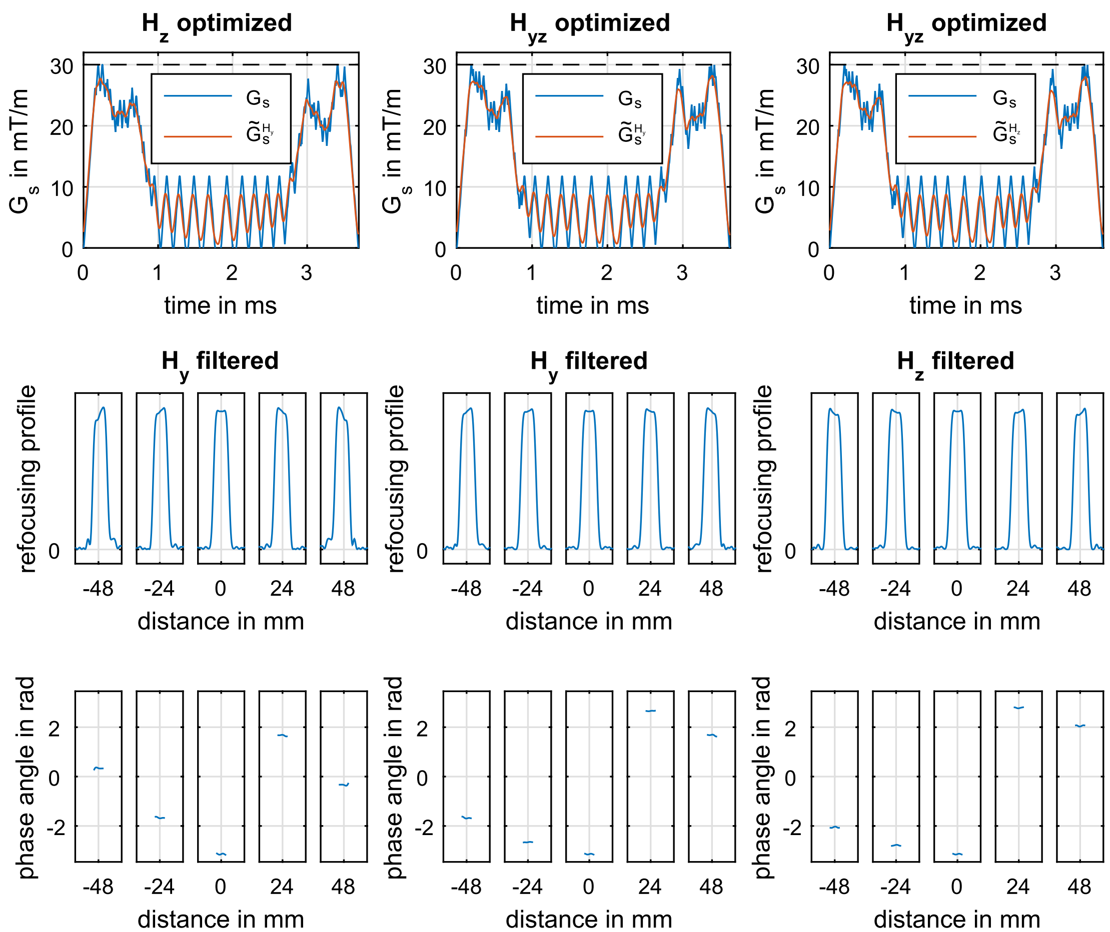

FIGURE 5 Comparison of 2 H_z and H_{yz} optimized MB = 5 examples filtered for different GIRF directions before Bloch simulation. Column 1 shows the H_y filtered result for the H_z optimized example shown in Figure 5. Columns 2 and 3 show the H_y and H_z filtered result for the H_{yz} (average of H_y and H_z) optimized example. Row 2 shows an enlargement of 6 mm to demonstrate the simulated refocusing profiles $|b_{N_t}(z)|^2$ and Column 3 shows an enlargement of 6 mm to see the phase spread $\arg(b_{N_t}(z)^2)$ of each slice

TABLE 1 Performance of initial and optimized SMS refocusing pulses (MB = 5, TBWP = 4, THK = 2 mm and FOV = 120 mm) for different GIRF directions (H_y, H_z and H_{yz}) with and without constraints on the phase angle of the refocusing profiles

		Max $\vert e_s \vert$ a.u.	Max $\vert e_p \vert$ rad	SAR_e W/kg	T ms
Initial	**GIRF**	**0.010**	**0.015**	**0.61**	**16.14**
Without phase constraints	H_i optimized	0.944	1.108	1.84	3.29
	H_y optimized	0.182	1.539	1.98	3.76
	H_z optimized	0.020	2.263	1.93	3.58
	H_{yz} optimized	0.087	0.746	1.86	3.60
With phase constraints	H_i optimized	0.923	0.675	1.65	3.42
	H_y optimized	0.138	0.053	1.82	3.64
	H_z optimized	0.020	0.024	1.86	3.69
	H_{yz} optimized	0.069	0.031	1.89	3.63

All pulses are evaluated using the H_z GIRF filtered slice selective gradient $\tilde{G}_s^{H_z}$ to analyze the influence of the GIRF direction. Depicted are the GIRF used in the optimization, maximal refocusing profile (e_s) and phase (e_p) errors, the SAR estimate (SAR_e) and the overall pulse duration (T). Examples of this table are also used in Figures 4 and 5 for further analysis.

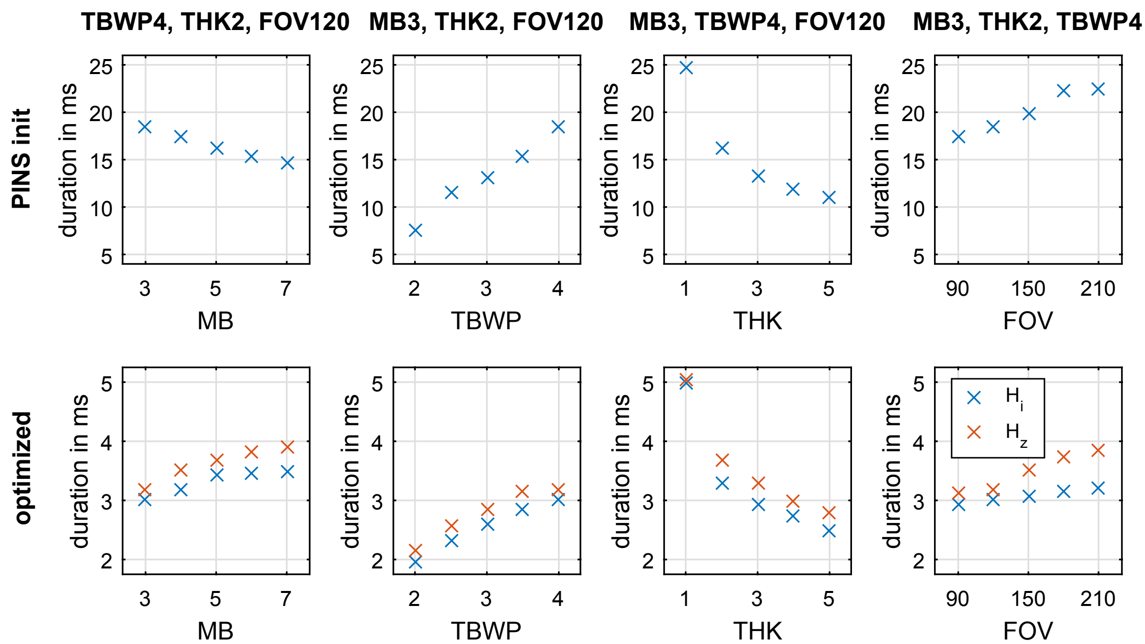

FIGURE 6 Overview of the initial PINS and the H_i and H_z optimized pulse durations for a variation of different parameters including time bandwidth product (TBWP), multiband factor (MB), slice thickness (THK), and field of view (FOV). A more detailed overview and description of the different examples is given in Supporting Information Figures S1-S4 and Supporting Information Table S2

GIRF-corrected pulse design method. The optimization robustly computed short pulse candidates that fulfilled all prescribed constraints. The performance of all H_i and H_z optimized results are summarized in Figure 6 showing the optimized pulse durations in comparison with the PINS pulse durations. More details of all optimized examples are given in Supporting Information Table S2 and Supporting Information Figures S1-S4. For the sake of clarity, the following results were documented for the H_z optimized results only since the H_i optimized results behave similarly. The pulse duration of the optimized results ranged from 3.19 ms to 3.90 ms (MB = 3-7), 2.16 ms to 3.19 ms (TBWP = 2-4), 2.78 ms to 5.04 ms (THK = 1-5 mm) and 3.12 ms to 3.84 ms (FOV = 90-210 mm). Supporting Information Figures S1-S4 depict 3 optimized results for each parameter variation. The average computation time of all H_i and H_z optimized pulses is approximately 30 minutes on the hardware described above.

4.2 | Experiments

Figure 7 shows the simulated and experimentally measured SE profiles on scanner 1 for 3 H_i and H_z optimized refocusing pulses with varying MB factor (3, 4 and 5). Results related to MB = 4 are also shown in Figure 2. The measured slice profile of all experiments matched simulated results and showed the expected slice profile distortions for the H_i optimized candidates. These distortions are corrected in the case of H_z optimization.

Figure 8 shows acquired in vivo gradient echo (GRE) images. As previously mentioned, the H_i and H_z optimized RF pulses were scaled to enable their use as low tip excitation pulses and to perform the scans on a scanner 2 with a GIRF not identical but close to H_z. Supporting Information Figure S5 shows the expected performance of the 9x-downscaled RF pulses in the excitation regime using the GIRF of scanner 1. The simulated excitation profiles were evaluated in terms of the flip angle $\sin^{-1}(|2a_{N_t}(z)b_{N_t}(z)^*|)$. The inclusion of the GIRF compensates slice profile distortions and results in clean slice profiles with a flip angle of 20°. Compared to Figure 2 there is an increased but still moderate error below 3%. The predicted signal recovery of the outer slices is in good accordance with the observed in vivo results. The reconstructed and separated in-vivo images on scanner 2 show a clear signal reduction for the outer slices, which is compensated using the H_z optimized waveforms. Furthermore, the H_z optimized waveforms have the advantage of reduced residual slices outside the field of view (not shown). The residual slices of the H_i optimized pulses resulted in signal crosstalk, as displayed in the center of the third slice (Figure 8). In contrast, the use of H_z optimized waveforms results in the desired consistent signal intensity.

5 | DISCUSSION

The inclusion of system specific hardware and safety constraints allows direct design of short SMS refocusing pulses to reduce T_E or echo spacing of existing clinically relevant SE sequences.[8] The achieved accuracy of highly fluctuating time optimal slice selective gradient shapes further depends on the performance of the gradient system and leads to the desired results only for gradient systems with a sufficiently high bandwidth.[22] In this work, we therefore presented an extension of the optimal control framework[21,22] to correct for spatially linear gradient system imperfections in the pulse design. The inclusion of a measured GIRF[23] in the optimization framework resulted in pre-emphasized G_s shapes that compensate for gradient system imperfections and that can be implemented without additional post-processing. The proposed framework is flexible in the optimization goal and allows for a tailored balance between a short pulse duration, small slice profile deviations, and RF power requirements. The presented GIRF-corrected SMS pulse design method robustly delivered short refocusing pulses for a variety of design parameters (MB factors, TBWP, THK, and FOV).

The various SMS refocusing cases presented in this work are typical configurations where the minimal pulse duration is limited by peak RF, G_s and slew rate amplitudes as well as the overall RF power. The hardware constraints and the measured GIRF chosen matched the 3T MR system used for experimental validation. These constraint values are input parameters and can be adapted to match different MR hardware. To achieve the best results with respect to the minimal pulse duration and refocusing accuracy it is therefore highly recommended to use the vendor specific hardware limitations and a GIRF that describes the gradient system and direction used.

The GIRF model predicts the actual slice selective gradient shape $\tilde{G}_s$ generated inside of the MR scanner's bore for a given demanded G_s shape.[23] In contrast to an idealized GIRF H_i, the low-pass character of the measured H_y and H_z, see Figure 1, suppresses higher frequency components and results in smoothed G_s shapes. It is important to mention that the GIRF models the gradient transfer function of a specific scanner model and gradient direction. Therefore, the GIRF varies for different gradient directions and substantially between models and vendors. Additional phase delays further result in temporal mismatches between RF and $\tilde{G}_s$ shape. As a consequence, the refocusing pattern is changed and the refocusing accuracy may be reduced for highly varying G_s shapes. The GIRF alterations can be iteratively corrected for a given RF and G_s shape[33] or reduced limiting the G_s frequency content.[17] These methods, however, do not guarantee compliance with respect to the hardware constraints. Alternatively, the presented direct inclusion of the measured GIRF in the optimization compensated for gradient imperfections and resulted in a matched RF pulse that is linked to the filtered slice selective gradient shape $\tilde{G}_s$. Moreover, the unfiltered G_s shapes are designed to exactly fulfill the prescribed hardware constraints to avoid any additional rescaling. We did not face any stability problems related to the use of an inverted GIRF in any of our optimization runs. The experiments show that this is beneficial for the practical performance of highly modulated slice selective gradient shapes in the presence of a limited gradient bandwidth.

To avoid additional known RF distortions associated with rapidly varying complex-valued RF pulses[32] we designed real valued RF pulses. In addition, we used the minimal gradient raster time of the MR system used for experimental validation (τ = 6.4 ms) to define both G_s and RF waveform. Since the RF amplifier system is expected to have a much higher bandwidth compared to the gradient system, we did not expect significant alteration of the optimized RF shapes. We also assumed an idealized RF system for all experiments. It would be straightforward to include LTI RF system imperfections into the optimization framework analogously to the GIRF model, or to include additional slew rate constraints on the RF amplitude. For all our experiments we utilized the existing vendor RF non-linearity correction prescan, which updated

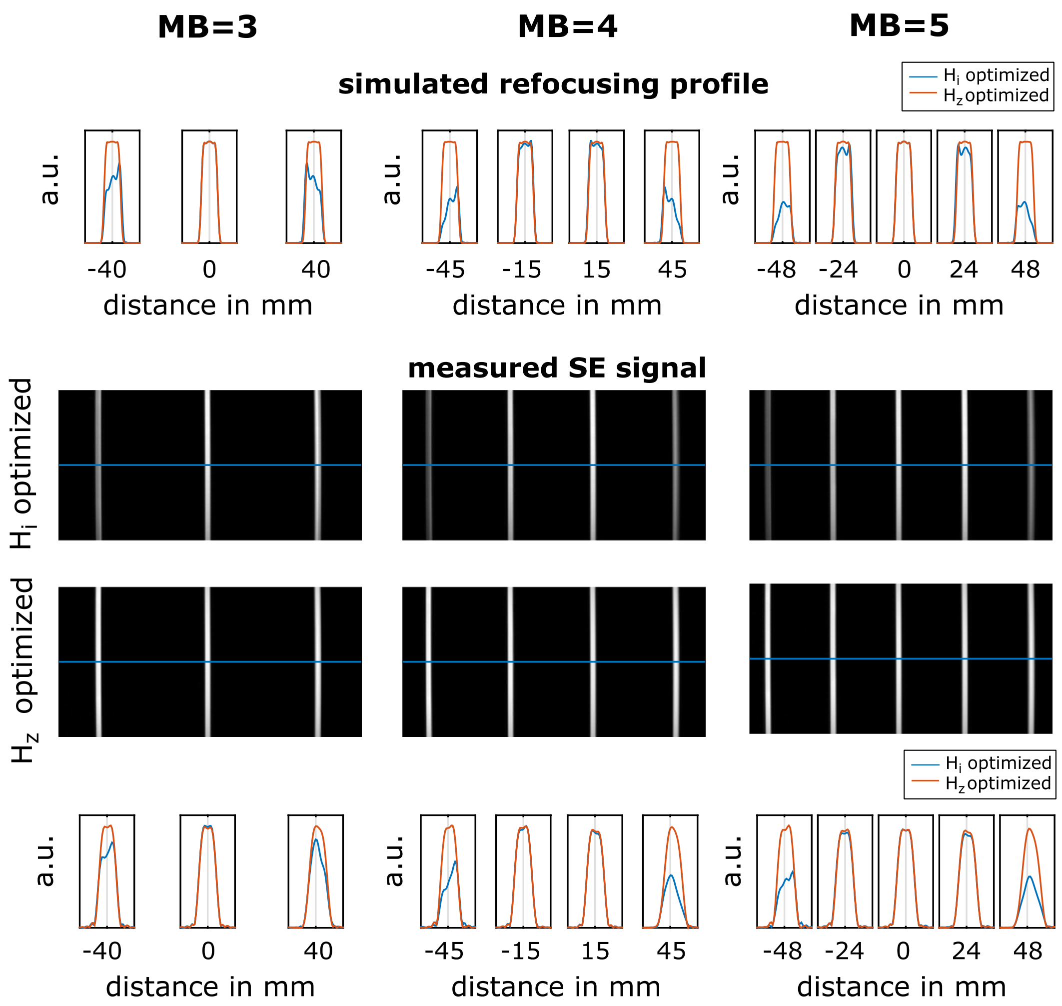

FIGURE 7 Simulated and measured SE phantom data of H_i (blue) and H_z (orange) optimized MB = 3, MB = 4, see Figure 2, and MB = 5 results on scanner 1. The first and last row shows an enlargement of 6 mm of the simulated and measured slice profiles

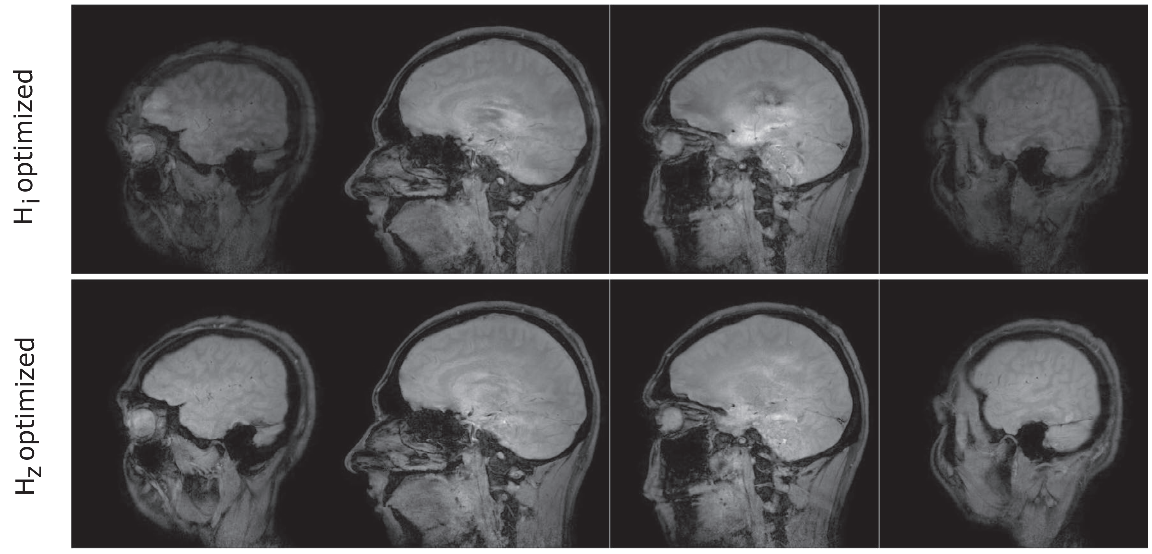

FIGURE 8 Reconstructed in vivo GRE acquisitions on scanner 2 using scaled MB = 4 RF pulses, see Figure 2, to achieve a nominal flip angle of 20∘. The H_i optimized RF pulses result in distorted slice profiles of the outer slices, which lead to a reduction in acquired signal. The H_z optimized RF pulses correct for this and consistent signal is achieved in all 4 slices

RF waveforms on a per scan basis. The residual imperfections in the RF waveforms were not directly measured, however, recently developed methods could be employed for this purpose and utilized to further refine the pre-compensation of RF waveforms.[34,35]

The optimization of all shown examples started with PINS[18] RF pulses and blipped G_s shapes that fulfill all given constraints. The use of PINS initials proved robust at yielding short pulse candidates for a large variation of parameters. This is in good accordance with our previous work on the design of SMS refocusing pulses without GIRF correction.[22]

Two representative cases (MB = 4 and MB = 5) were investigated in more detail. The low-pass character and the frequency dependent phase delay of H_z resulted in a smoothed and partly time-shifted slice selective gradient shape. These alterations changed the temporal alignment with the optimized RF shape and resulted in degraded slice profiles, especially for the slices farther away from the isocenter. In contrast, there was a much smaller discrepancy in the refocusing profile closer to the isocenter. These alterations, however, could be corrected with the proposed H_z GIRF incorporation during the optimization. Interestingly, the unfiltered G_s shapes optimized with the ideal and measured GIRF had a similar visual appearance and a comparable frequency range. The still high slice selective gradient fluctuations come with the disadvantage of an increased gradient demand and mechanical vibrations. However, we did not face any problems with peripheral nerve stimulation in any of our experimental scans.

The inclusion of H_z created a pre-distorted slice selective gradient shape that compensates the GIRF low-pass and phase characteristics and removed the undesired slice profile degradations.

This clear advantage comes with a price of slightly increased minimal pulse durations and SAR estimates. It should be noted, that the optimized global head SAR estimate is far from the used global head SAR constraint of 3.2 W/kg. The unconstrained phase spread problem has more freedom and therefore more local solutions with a shorter pulse duration. However, there is only a minor increase in the pulse duration when adding explicit phase spread constraints to each refocusing slice. Moreover, the combination of explicit phase constraints and H_z resulted in only a slightly longer pulse duration with a vast reduction compared to the initial guess.

The robustness of the H_z filtered initial guess and optimized pulses (MB = 4) with respect to time invariant and static B_0 and B_1 variations were investigated after the iterative design process with numerical Bloch simulations, see Figure 3. The reduced durations of the optimized pulses lead to lower slice displacement, but a higher B_0 sensitivity as a result of the variable k-space velocity. The H_z optimized and H_z filtered results provide stable refocusing profiles in the range of ±150 Hz, which is in good agreement with time optimal results that assumed an idealized GIRF.[22] Depending on the application more robust pulses may be required. Therefore, an inclusion of B_0/B_1 robustness into the optimization framework will be focus of future work.

The different gradient coil design of longitudinal (z-direction) and transversal (y-direction) leads to a slightly different GIRF for each direction. To achieve the best accuracy, the GIRF used in the optimization should fit with the gradient direction of the MR experiment. Nevertheless, there are only small differences between H_y and H_z, see Figure 1. This directly translated to the numerical Bloch simulations using a different GIRF for optimization and simulation with only small slice profile deviations, see Figure 5. If the gradient direction is unknown prior to optimization, an averaged GIRF of different gradient directions could be used. This intermediate case results in smaller maximal slice profile deviations compared to use of a single distinct GIRF in the optimization and evaluation.

For validation we have performed 2 different experiments on 2 different MR systems of the same model. The phantom experiments clearly show the beneficial effects of the incorporated GIRF correction. Because of software limitations we used the GIRF measured from 1 MR system to correct pulses applied to another. The in vivo demonstration was further limited to gradient echo measurements. To comply with this restriction we used 9x-downscaled refocusing pulses and applied them as excitation pulses. The performance of the scaled pulses was estimated with Bloch simulations in the excitation regime ($|2ab^*|$). Although the pulses were designed with respect to the crushed refocusing profile ($|b^2|$) it is reasonable to expect clean excitation slice profiles. Moreover, distorted slice profiles are recovered using the proposed design method. This is in good accordance with the observed in vivo results acquired on system 2. The good experimental performance implies that the gradient systems do have similar frequency responses, which we have observed before.[17] However, more work is needed to understand the limits of using generic GIRFs to improve the applicability of the proposed method.

The proposed GIRF compensated design method was tested for various parameters including different MB factors (3−8), TBWP (2−4), THK (1−5 mm), FOV (90−210 mm), phase angle constraints and gradient directions.

In addition to the uniform signal strength, the GIRF-corrected pulse design results in an additional reduction of residual slices outside the FOV. This reduction of aliased slices is in agreement with previously published work.[17]

The proposed method provides a new approach for GIRF-corrected RF pulse design. The incorporation of the GIRF into the optimization framework generates a pre-emphasized G_s shape and a matched RF pulse that can be applied to further push the limits of SMS sequences such as clinically important turbo spin echo (TSE) based sequences,[36] functional imaging[37] or short SE diffusion applications.[38]

6 | CONCLUSIONS

The inclusion of a hardware specific GIRF into the optimal control framework provides compensation of limited gradient performance and yields distinct refocusing slices, even for minimum duration RF and rapidly changing Gs shapes.

ACKNOWLEDGMENTS

Partial support from "SFB F32-N18" and BioTechMed-Graz are gratefully acknowledged. This work was supported by the Wellcome Trust/EPSRC Centre for Medical Engineering at King's College London [WT 203148/Z/16/Z]; the National Institute for Health Research (NIHR) Biomedical Research Centre based at Guy's and St Thomas' NHS Foundation Trust and King's College London. The views expressed are those of the author(s) and not necessarily those of the NHS, the NIHR or the Department of Health. This work is funded by the King's College London & Imperial College London EPSRC Centre for Doctoral Training in Medical Imaging [EP/L015226/1] and [EP/L00531X/1]. Karl Kunisch was partially supported by the ERC advanced grant 668998 (OCLOC) under the EUs H2020 research program.

ORCID

Christoph S. Aigner http://orcid.org/0000-0003-3618-9610
Armin Rund http://orcid.org/0000-0001-7934-4970
Samy Abo Seada http://orcid.org/0000-0003-3221-433X
Anthony N. Price http://orcid.org/0000-0002-6907-7554
Shaihan J. Malik http://orcid.org/0000-0001-8925-9032

REFERENCES

1. Tsao J. Ultrafast imaging: principles, pitfalls, solutions, and applications. *J Magn Reson Imaging*. 2010;32:252–266.
2. Blaimer M, Breuer F, Mueller M, Heidemann RM, Griswold MA, Jakob PM. SMASH, SENSE, PILS, GRAPPA: how to choose the optimal method. *Topics Magn Reson Imaging*. 2004;15:223–236.
3. Deshmane A, Gulani V, Griswold MA, Seiberlich N. Parallel MR imaging. *J Magn Reson Imaging*. 2012;36:55–72.
4. Feinberg DA, Setsompop K. Ultra-fast MRI of the human brain with simultaneous multi-slice imaging. *J Magn Reson*. 2013;229:90–100.
5. Barth M, Breuer F, Koopmans P, Norris D, Poser B. Simultaneous multislice (SMS) imaging techniques. *Magn Reson Med*. 2016;75:63–81.
6. Mueller S. Multifrequency selective RF pulses for multislice MR imaging. *Magn Reson Med*. 1988;6:364–371.
7. Norris DG, Boyacioglu R, Schulz J, Barth M, Koopmans PJ. Application of PINS radiofrequency pulses to reduce power deposition in RARE/turbo spin echo imaging of the human head. *Magn Reson Med*. 2014;71:44–49.
8. Grissom WA, Setsompop K, Hurley SA, Tsao J, Velikina JV, Samsonov AA. Advancing RF pulse design using an open-competition format: report from the 2015 ISMRM challenge. *Magn Reson Med*. 2017;78:1352–1361.
9. Wong E. Optimized phase schedules for minimizing peak RF power in simultaneous multi-slice RF excitation pulses. In Proceedings of the International Society for Magnetic Resonance in Medicine, Melbourne, Australia, 2012. Abstract #2209.
10. Auerbach EJ, Xu J, Yacoub E, Moeller S, Uğurbil K. Multiband accelerated spin-echo echo planar imaging with reduced peak RF power using time-shifted RF pulses. *Magn Reson Med*. 2013;69:1261–1267.
11. Sharma A, Lustig M, Grissom WA. Root-flipped multiband refocusing pulses. *Magn Reson Med*. 2016;75:227–237.
12. Conolly S, Nishimura D, Macovski A, Glover G. Variable-rate selective excitation. *J Magn Reson*. 1988;78:440–458.
13. Hargreaves BA, Cunningham CH, Nishimura DG, Conolly SM. Variable-rate selective excitation for rapid MRI sequences. *Magn Reson Med*. 2004;52:590–597.
14. Setsompop K, Gagoski BA, Polimeni JR, Witzel T, Wedeen VJ, Wald LL. Blipped-controlled aliasing in parallel imaging for simultaneous multislice echo planar imaging with reduced g-factor penalty. *Magn Reson Med*. 2012;67:1210–1224.
15. Grissom WA, McKinnon GC, Vogel MW. Nonuniform and multidimensional Shinnar-Le Roux RF pulse design method. *Magn Reson Med*. 2012;68:690–702.
16. Kobayashi N, Ugurbil K, Wu X. Shortening nonlinear phase multiband refocusing pulses with VERSE. In Proceedings of the International Society for Magnetic Resonance in Medicine, Singapore, Republic of Singapore, 2016. Abstract #3253.
17. Abo Seada S, Price AN, Schneider T, Hajnal JV, Malik SJ. Multiband RF pulse design for realistic gradient performance. *Magn Reson Med*. 2019;81:362–376.
18. Norris DG, Koopmans PJ, Boyacioğlu R, Barth M. Power independent of number of slices (PINS) radiofrequency pulses for low-power simultaneous multislice excitation. *Magn Reson Med*. 2011;66:1234–1240.
19. Eichner C, Wald LL, Setsompop K. A low power radiofrequency pulse for simultaneous multislice excitation and refocusing. *Magn Reson Med*. 2014;72:949–958.
20. Aigner CS, Clason C, Rund A, Stollberger R. Efficient high-resolution RF pulse design applied to simultaneous multi-slice excitation. *J Magn Reson*. 2016;263:33–44.
21. Rund A, Aigner CS, Kunisch K, Stollberger R. Magnetic resonance RF pulse design by optimal control with physical constraints. *IEEE Trans Med Imaging*. 2018;37:461–472.
22. Rund A, Aigner CS, Kunisch K, Stollberger R. Simultaneous multislice refocusing via time optimal control. *Magn Reson Med*. 2018;80:1416–1428.
23. Vannesjo SJ, Haeberlin M, Kasper L, et al. Gradient system characterization by impulse response measurements with a dynamic field camera. *Magn Reson Med*. 2013;69:583–593.
24. Campbell-Washburn AE, Xue H, Lederman RJ, Faranesh AZ, Hansen MS. Real-time distortion correction of spiral and echo planar images using the gradient system impulse response function. *Magn Reson Med*. 2016;75:2278–2285.
25. Cavusoglu M, Mooiweer R, Pruessmann KP, Malik SJ. VERSE-guided parallel RF excitations using dynamic field correction. *NMR Biomed*. 2017;30:e3697.
26. Harkins KD, Does MD, Grissom WA. Iterative method for predistortion of MRI gradient waveforms. *IEEE Trans Med Imaging*. 2014;33:1641–1647.
27. Busch J, Vannesjo SJ, Barmet C, Pruessmann KP, Kozerke S. Analysis of temperature dependence of background phase errors in phase-contrast cardiovascular magnetic resonance. *J Cardiovasc Magn Reson*. 2014;16:1–12.

28. Jaynes E. Matrix treatment of nuclear induction. *Phys Rev*. 1955;98:1099–1105.
29. Pauly J, Le Roux P, Nishimura D, Macovski A. Parameter relations for the Shinnar–Le Roux selective excitation pulse design algorithm. *IEEE Trans Med Imaging*. 1991;10:53–65.
30. Vernickel P, Röschmann P, Findeklee C, et al. Eight-channel transmit/receive body MRI coil at 3T. *Magn Reson Med*. 2007;58:381–389.
31. Papadakis NG, Wilkinson AA, Carpenter T, Hall LD. A general method for measurement of the time integral of variant magnetic field gradients: application to 2D spiral imaging. *Magn Reson Imaging*. 1997;15:567–578.
32. Abo Seada S, Price AN, Hajnal JV, Malik SJ. Optimized amplitude modulated multiband RF pulse design. *Magn Reson Med*. 2017;78:2185–2193.
33. Abo Seada S, Hajnal JV, Malik SJ. A simple optimisation approach to making time efficient verse-multiband pulses feasible on non-ideal gradients. In Proceedings of the 25th Annual Meeting of ISMRM, Honolulu, HI, 2017. Abstract #5049.
34. Landes VL, Nayak KS. Simple method for RF pulse measurement using gradient reversal. *Magn Reson Med*. 2018;79:2642–2651.
35. Landes VL, Nayak KS. Improved multi-band RF performance using GRATER-based predistortion. In Proceedings of the 26th Annual Meeting of ISMRM, France, 2018. Abstract #0171.
36. Gagoski BA, Bilgic B, Eichner C, et al. RARE/turbo spin echo imaging with simultaneous multislice Wave-CAIPI. *Magn Reson Med*. 2015;73:929–938.
37. Chen L, Vu AT, Xu J, et al. Evaluation of highly accelerated simultaneous multi-slice EPI for fMRI. *NeuroImage*. 2015;104:452–459.
38. Setsompop K, Fan Q, Stockmann J, et al. High-resolution in vivo diffusion imaging of the human brain with generalized slice dithered enhanced resolution: simultaneous multislice (gSlider-SMS). *Magn Reson Med*. 2018;79:141–151.

SUPPORTING INFORMATION

Additional supporting information may be found online in the Supporting Information section at the end of the article.

FIGURE S1 Comparison of optimized results with different MB factors (3–7) with fixed THK = 2 mm, TBWP = 4 and FOV = 120 mm. Row 1 shows the optimized slice selective gradient shapes before (G_s) and after convolution with the GIRF ($\tilde{G}_s^{H_z}$). Row 2 shows an enlargement of 4 mm of the simulated refocusing profiles $|b(z)|^2$ and row 3 shows the phase angle $\arg(b_{N_t}(z)^2)$ of each slice (range of 4 mm) after GIRF convolution

FIGURE S2 Comparison of optimized results with different TBWP factors (2.5-3.5) with fixed MB = 3, THK = 2 mm and FOV = 120 mm. Row 1 shows the optimized slice selective gradient shapes before (G_s) and after convolution with the GIRF ($\tilde{G}_s^{H_z}$). Row 2 shows an enlargement of 4 mm of the simulated refocusing profiles $|b(z)|^2$ and row 3 shows the phase angle $\arg(b_{N_t}(z)^2)$ of each slice (range of 4 mm) after GIRF convolution

FIGURE S3 Comparison of optimized results with different THK (5-1 mm) with fixed MB = 5, TBWP = 4 and FOV = 120 mm. Row 1 shows the optimized slice selective gradient shapes before (G_s) and after convolution with the GIRF ($\tilde{G}_s^{H_z}$). Row 2 shows an enlargement of 8 mm of the simulated refocusing profiles $|b(z)|^2$ and row 3 shows the phase angle $\arg(b_{N_t}(z)^2)$ of each slice (range of 8 mm) after GIRF convolution

FIGURE S4 Comparison of optimized results with different field of view (FOV = 90-210 mm) with fixed MB = 3, TBWP = 4 and THK = 2 mm. Row 1 shows the optimized slice selective gradient shapes before (G_s) and after convolution with the GIRF ($\tilde{G}_s^{H_z}$). Row 2 shows an enlargement of 4 mm of the simulated refocusing profiles $|b(z)|^2$ and row 3 shows the phase angle $\arg(b_{N_t}(z)^2)$ of each slice (range of 4 mm) after GIRF convolution

FIGURE S5 Simulated excitation profiles of 9x-downscaled H_i and H_z optimized refocusing pulses, shown in Figure 2. The excitation profiles are depicted in terms of the flip angle $\sin^{-1}(|2a_{N_t}(z)b_{N_t}(z)^*|)$. Note that despite the pulses have been optimized with respect to the refocusing profile $|b_{N_t}(z)|^2$ the 9x-downscaled pulses result in clean slice profiles with a 20° flip angle. The pulses are evaluated using the H_z GIRF (scanner 1) filtered slice selective gradient $\tilde{G}_s^{H_z}$. The H_z optimized pulse recovers the lower signal of the outer slices which is in accordance with the observed invivo results in Figure 8

TABLE S1 Performance of optimized SMS refocusing pulses (MB = 5, TBWP = 4, THK = 2 mm and FOV = 120 mm) for different GIRF directions (H_y, H_z and H_{yz}) with and without constraints on the phase angle of the refocusing profiles. All pulses are evaluated using the H_y and H_{yz} GIRF filtered slice selective gradient $\tilde{G}_s^{H_z}$ and $\tilde{G}_s^{H_{yz}}$ to analyze the influence of the GIRF direction. Depicted are the GIRF used in the optimization, maximal refocusing profile (e_s) and phase (e_p) errors

TABLE S2 Performance of initial and optimized results with varying TBWP = 2-4, MB= 3-8 factor, THK = 1-5 mm and FOV = 90-210 mm. The optimization is done with the measured GIRF along the *z*-direction (H_z) with explicit phase constraints. The slice and phase errors are evaluated after Bloch simulation with the GIRF filtered slice selective gradient shape $\tilde{G}_s^{H_z}$. Parameters used: maximal refocusing slice (e_s) and phase (e_p) errors, the SAR estimate (SAR_e) and the overall pulse duration (T)

How to cite this article: Aigner CS, Rund A, Abo Seada S, et al. Time optimal control-based RF pulse design under gradient imperfections. *Magn Reson Med*. 2020;83:561–574. https://doi.org/10.1002/mrm.27955